Suomi satellite brings to light a unique frontier of nighttime environmental sensing capabilities

Steven D. Miller[a,1], Stephen P. Mills[b], Christopher D. Elvidge[c], Daniel T. Lindsey[d], Thomas F. Lee[e], and Jeffrey D. Hawkins[e]

[a]Cooperative Institute for Research in the Atmosphere, Colorado State University, Fort Collins, CO 80523; [b]Northrop Grumman Aerospace Systems, Redondo Beach, CA 90278; [c]National Geophysical Data Center, National Oceanic and Atmospheric Administration, Boulder, CO 80305; [d]Regional and Mesoscale Meteorology Branch, Center for Satellite Applications and Research, National Environmental Satellite, Data, and Information Service, National Oceanic and Atmospheric Administration, Fort Collins, CO 80523; and [e]Satellite Meteorological Applications Section, Marine Meteorology Division, Naval Research Laboratory, Monterey, CA 93943

Edited by Michael Mishchenko, National Aeronautics and Space Administration Goddard Institute, New York, NY, and accepted by the Editorial Board August 10, 2012 (received for review April 25, 2012)

Most environmental satellite radiometers use solar reflectance information when it is available during the day but must resort at night to emission signals from infrared bands, which offer poor sensitivity to low-level clouds and surface features. A few sensors can take advantage of moonlight, but the inconsistent availability of the lunar source limits measurement utility. Here we show that the Day/Night Band (DNB) low-light visible sensor on the recently launched Suomi National Polar-orbiting Partnership (NPP) satellite has the unique ability to image cloud and surface features by way of reflected airglow, starlight, and zodiacal light illumination. Examples collected during new moon reveal not only meteorological and surface features, but also the direct emission of airglow structures in the mesosphere, including expansive regions of diffuse glow and wave patterns forced by tropospheric convection. The ability to leverage diffuse illumination sources for nocturnal environmental sensing applications extends the advantages of visible-light information to moonless nights.

airglow/nightglow | nocturnal remote sensing

The sky on a dark, moonless night is, in fact, immersed within a sea of visible-spectrum light that the dark-adjusted human eye can only begin to discern. The primary sources are the polar aurora, airglow, integrated starlight (including the Milky Way), and zodiacal light (1–3). Auroras, although a relatively strong source, are ephemeral and confined to high latitudes. The other sources produce a complex global distribution of nighttime diffuse sky brightness that varies considerably across space, time, and spectrum. At visible and near infrared wavelengths (e.g., 0.4–1.1 μm), the combined illumination from these sources yields down-welling radiances at Earth's surface in the range $\sim 10^{-11}$ to 10^{-9} $W \cdot cm^{-2} \cdot sr^{-1} \cdot \mu m^{-1}$ (3), or approximately 1 billion times fainter than sunlight.

Low-light imaging capabilities have existed on the Operational Linescan System (OLS) on the Defense Meteorological Satellite Program (DMSP) constellation since the late 1960s. The OLS was designed to amplify visible light and detect clouds under twilight and moonlight (e.g., signals down to $\sim 10^{-8}$ $W \cdot cm^{-2} \cdot sr^{-1} \cdot \mu m^{-1}$) illumination conditions (4) but soon revealed many additional capabilities based on signals from both natural and anthropogenic sources (5–8).

The Suomi National Polar-orbiting Partnership (NPP) satellite (http://npp.gsfc.nasa.gov) was launched on October 28, 2011, and placed into an 834-km altitude sun-synchronous orbit with local equatorial crossing times of ~1:30 PM and 1:30 AM. Named in honor of Verner E. Suomi, considered widely as the "father of satellite meteorology," NPP provides risk reduction for the Joint Polar Satellite System (JPSS) series of National Oceanic and Atmospheric Administration (NOAA) operational meteorological satellites and continuity to the National Aeronautics and Space Administration (NASA) Earth Observing System (EOS) Terra and Aqua climate research satellites (9).

Suomi NPP carries the Visible/Infrared Imager/Radiometer Suite (VIIRS), an optical spectrum (22 bands spanning ~0.4–13 μm) sensor providing imagery at high spatial resolution (0.375–1.6 km, band dependent) across a 3,000-km-wide swath. Included on VIIRS is a next-generation low-light sensor, the Day/Night Band (DNB). The DNB has a measured spectral response of 505–890 nm (full width at half maximum, with nominal band-center wavelength of 705 nm) and features several advances to the heritage OLS, including full calibration and improved spatial (0.74 km vs. ~3 km) and radiometric (14-bit vs. 6-bit) resolutions (10). Three stages of gain allow the DNB to span the dynamic range of radiances encountered during the daytime, twilight, and nighttime with measured radiometric uncertainties of 3.5%, 7.8%, and 11.0%, respectively. The data are calibrated and spectrally normalized with respect to an on-board solar diffuser, which has a reflectance that is monitored for stability. Noise-equivalent radiance increases from $\sim 1 \times 10^{-10}$ $W \cdot cm^{-2} \cdot sr^{-1}$ at nadir to $\sim 3 \times 10^{-10}$ $W \cdot cm^{-2} \cdot sr^{-1}$ at scan edge.

The current findings came about unexpectedly during routine instrument check-out procedures for the VIIRS/DNB. To characterize and remove sensor noise and offset patterns, we examined astronomically dark scenes over the open oceans during nights around the new moon (i.e., completely devoid of sunlight, moonlight, and anthropogenic light contamination). Upon first inspection of these data, the noise pattern was found to contain irregularly distributed structures. The anomalous structures were discovered to be meteorological clouds (Fig. 1) illuminated by an unanticipated source of visible light.

Sources of Night Sky Brightness and Relative Magnitudes

A complete description of the nonlunar nighttime illumination sources can be found in the reviews of refs. 1 and 3. We shall limit our discussion here to the globally ubiquitous sources (namely airglow, starlight, and zodiacal light), referring to these collectively as "diffuse illumination, multisource" (or "DIM") emissions of nighttime visible light.

The zodiacal light (11) arises from sunlight scattered by interplanetary dust in the solar system. Because this dust is concentrated along the ecliptic and increases in density with proximity to the Sun, there is a strong spatial structure to this source (ref. 3, figure 37). At high elongation angles from the Sun (i.e., near local midnight, approximately the time of the Suomi NPP overpass), this

Author contributions: S.D.M. designed research; S.D.M. performed research; S.D.M., S.P.M., and C.D.E. contributed new reagents/analytic tools; S.D.M., S.P.M., C.D.E., D.T.L., T.F.L., and J.D.H. analyzed data; and S.D.M., S.P.M., and T.F.L. wrote the paper.

The authors declare no conflict of interest.

This article is a PNAS Direct Submission. M.M. is a guest editor invited by the Editorial Board.

Freely available online through the PNAS open access option.

[1]To whom correspondence should be addressed. E-mail: steven.miller@colostate.edu.

This article contains supporting information online at www.pnas.org/lookup/suppl/doi:10.1073/pnas.1207034109/-/DCSupplemental.

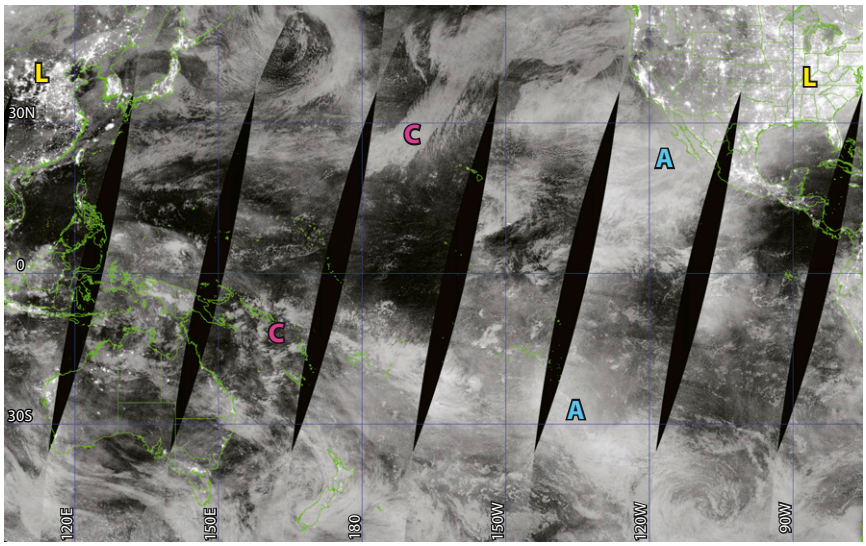

Fig. 1. Low-light imagery from a series of adjacent Suomi NPP VIIRS/DNB nighttime passes over the Pacific Ocean on the night of February 22, 2012. The coverage domain spans 20,000 km east-to-west and 12,500 km north-to-south, with geopolitical boundaries drawn in green. The data were collected during new moon conditions (no sunlight or moonlight present). In addition to city light emissions (e.g., L), the observations capture clouds (e.g., C) illuminated by reflected airglow, starlight, and zodiacal light. Also apparent are broad, diffuse regions of primary airglow emission (e.g., A).

light source is minimized, with an expected 640-nm radiance range spanning roughly 0.4–1.1 × 10^{-10} W·cm^{-2}·sr^{-1}·μm^{-1} (from ecliptic poles to equator, respectively).

Starlight is composed mainly of contributions from the ∼8,500 visible stars and the integrated light from the ∼10^{11} subvisible stars of the Milky Way. The brightness of the galactic source is highly variable (12), with the largest values along the galactic equator and significantly smaller values at the poles (ref. 3, table 36). Consequently the magnitude of this source varies over the course of the year, smallest in December and peaking in July. The combined starlight source produces 640-nm radiances in the range of roughly 1.8–4.0 × 10^{-10} W·cm^{-2}·sr^{-1}·μm^{-1}. Contributions from the diffuse scatter of galactic and cosmic light by interstellar dust are two orders of magnitude lower and considered here to be negligible.

Among the DIM sources, airglow dominates in terms of its magnitude, dynamic range, and space/time variability, and so receives special attention here. Airglow refers to the self-illumination of the upper atmosphere via chemiluminescence processes. Nocturnal airglow (called "night glow") results from the photoionization of atmospheric gases by ultraviolet (UV) sunlight. Night glow brightness ranges from 10^{-10} to 10^{-9} W·cm^{-2}·sr^{-1}·μm^{-1} (13) within the DNB sensor response when viewed from the surface and at local zenith. Whereas the OLS has not demonstrated the ability to produce useful meteorological imagery from the DIM sources, the slight red shift of the DNB sensor response (toward the significant near-infrared Meinel OH* airglow bands; see Fig. S1) makes it inherently more sensitive to these emissions.

At the surface, the airglow layer appears brightest (a factor of ∼4 larger than the zenith value) at an elevation angle of approximately 10° (the van Rhijn function, e.g., ref. 14). Airglow as seen from space has been documented from the Space Shuttle (15) and more recently from the International Space Station (ISS; http://eol.jsc.nasa.gov/Videos/CrewEarthObservationsVideos). Fig. 2, taken by astronauts on board the ISS, shows the relative brightness and distribution of several nocturnal light sources including the airglow layer.

Airglow Spectral/Space/Time Characteristics

Airglow emissions occur both as distinct bands and as continuum emission, spanning the UV through the visible and into the near infrared (16, 17). Significant contributions with respect to the DNB response include atomic oxygen at 557.7, 630, and 636 nm (altitudes between ∼250–300 km), atomic sodium at 589.0 and 589.6 nm, excited hydroxyl (OH*) radicals (500 nm out to 4.5 μm), and molecular oxygen from 761.9 nm (A-band) and 864.5 nm. The dominant OH* emission layer is geometrically thin (10–20 km), occurring around a critical air density at approximately 85 km where excited species are abundant and the favorable mechanism for energy dissipation is photon emission.

Airglow emissions are highly variable spatially, seasonally, and diurnally (18–20) and track changes in solar insolation, atmospheric density, and atomic oxygen availability. This behavior includes a semiannual oscillation in maxima with amplitude variations that are lower in the tropics and higher at midlatitudes (20–22). Regionally, the emissions produce complex transient banding or patch-like structures associated with planetary waves (23) and mesospheric tides (24, 25). At finer spatial scales, emission features are associated with ionospheric disturbances forced by atmospheric gravity waves (26, 27). The observed structures have been tied to tropospheric convection and seismic activity, with the latter proposed as a means for early detection of tsunamis (28).

Previous Measurements

The Orbiting Geophysical Observatory (OGO-4) provided the first global maps of the time-varying airglow distribution and intensity (19). More recent airglow monitoring sensors include the Wind Imaging Interferometer (WINDII; ref. 24), the Special Sensor UV Spectrographic Imager (SSUSI; ref. 29), the Optical Spectrograph IR imager (OSIRIS) limb-viewing camera (30), and the Thermosphere Ionosphere Mesosphere Energetics and Dynamics (TIMED) instrument (25). These sensors were designed to characterize upper atmospheric properties that influence high frequency communications and near-field sources of light contamination that impact astronomy, as opposed to meteorological applications.

Early photometer observations from OGO-4 suggested a possible meteorological utility of airglow (31), although the nonimaging and spatially coarse (∼100 km) nature of those measurements permitted only crude inference of transitions between low and high albedo features (e.g., crossing from ocean to desert). Similarly, the DMSP/SSUSI NPS (a nonimaging photometer) enlists a secondary measurement at 629.4 nm to

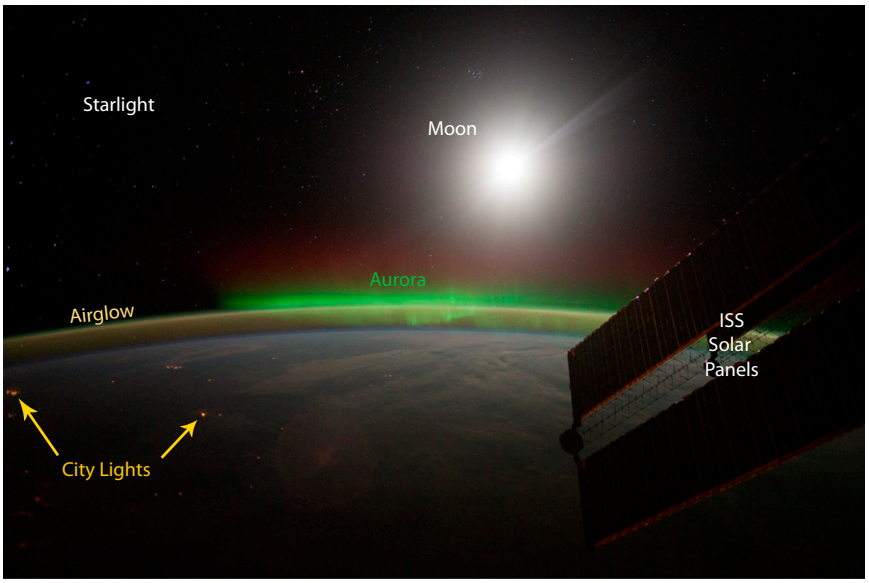

Fig. 2. Earth's limb as seen from the International Space Station on February 1, 2012, 06:11:39 UTC, over the northern Atlantic Ocean. The view is to the northeast, and shows qualitatively the relative brightness and distribution of various sources of nighttime illumination including airglow, the aurora borealis, the gibbous moon, starlight, and city lights. The lunar source is significantly brighter than the DIM sources, appearing like a star in this exposure. A solar panel from the ISS appears in the foreground. (Nikon D3s image ISS030-E-73400 courtesy of the Image Science and Analysis Laboratory, NASA Johnson Space Center).

characterize and remove background contributions from Earth's albedo. To date, the only documented use of nonsolar/lunar sources for cloud imaging comes from surface-based camera systems (32), based on cloud extinction of down-welling airglow emissions as opposed to cloud reflectance.

Example Imagery

Fig. 1 shows VIIRS/DNB cloud imagery over the Pacific Ocean from several consecutive nighttime passes in conditions completely devoid of both sunlight and moonlight. To avoid edge-of-scan noise effects, the data were cropped at a maximum sensor zenith angle of 60°, resulting in small coverage gaps between adjacent passes at lower latitudes. City lights appear as discrete, bright features. Additional examples are published (Figs. S2–S4).

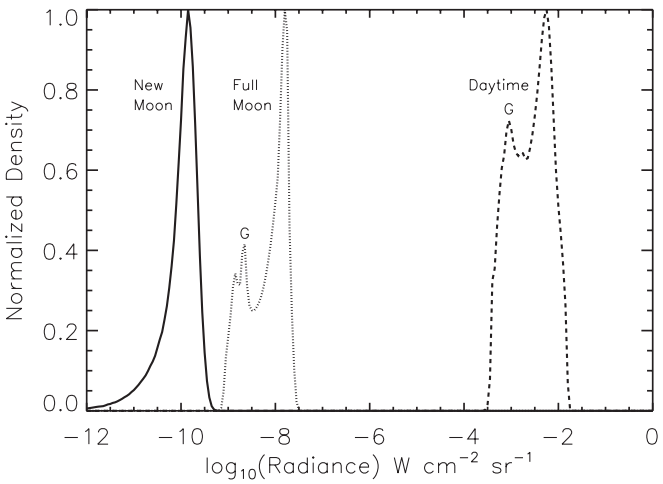

Fig. 3. Distributions of Suomi NPP VIIRS DNB-measured radiances over the north/central Pacific Ocean for nighttime new moon, full moon, and daytime scenes. The secondary low-radiance modes (G) of the full moon and daytime distributions are due to moon and sun glint (respectively) off the ocean surface—a characteristic not seen in the extended diffuse light sources.

To compare the relative brightness of various illumination sources, we produced normalized distributions of DNB radiance (in $W{\cdot}cm^{-2}{\cdot}sr^{-1}$) from the north/central Pacific Ocean during nighttime new moon (i.e., only DIM sources), nighttime full moon, and daytime overpasses. Fig. 3 shows that nighttime scenes illuminated by full moon are roughly 1 million times fainter than the daytime, and the new moon scenes are approximately 100 times fainter than full moon. Secondary modes in the full moon and daytime distributions correspond to lunar and solar glint (specular reflection off the ocean surface) regions, respectively.

Nighttime detection of low clouds and other near-surface features in the thermal infrared is problematic because of poor thermal contrast. Here, DIM light imagery offers distinct advantages. Fig. 4 compares VIIRS DNB and M15 (10.7 μm) observations of a low cloud layer over the northern Korean Peninsula. The western and northern edges of the low cloud field are difficult to discern over land in the infrared imagery but stand out readily in the DIM light imagery. The imagery also reveals details of the low cloud structure below optically thin cirrus.

Fig. 5 shows a DIM light image of a convective system over the Pacific Ocean. The lightning flash (which appears as a bright segment oriented along a DNB scan line, due to the scanning nature of the sensor) and convective clouds are features that could have been detected with heritage DMSP/OLS sensor. However, in addition to these features, the DNB reveals a train of mesospheric gravity waves in the primary airglow emission, originating from the area of convection and propagating away to the east/northeast.

Source Determination and Analysis

We considered the possibility that thermal emission might explain the cloud detections. Ground tests of the silicon-based DNB detectors showed no sensitivity to wavelengths > 0.91 μm, and even at this limit the levels of blackbody emission are vanishingly small—at least 10 orders of magnitude below minimum detection limits. Before the thermal infrared VIIRS bands are cooled to their 80 K operational temperature, any cross talk with the DNB would have manifested as white noise as opposed to the coherent structures observed, and the character of DNB imagery did not change as these bands were cooled. Further evidence against a thermal

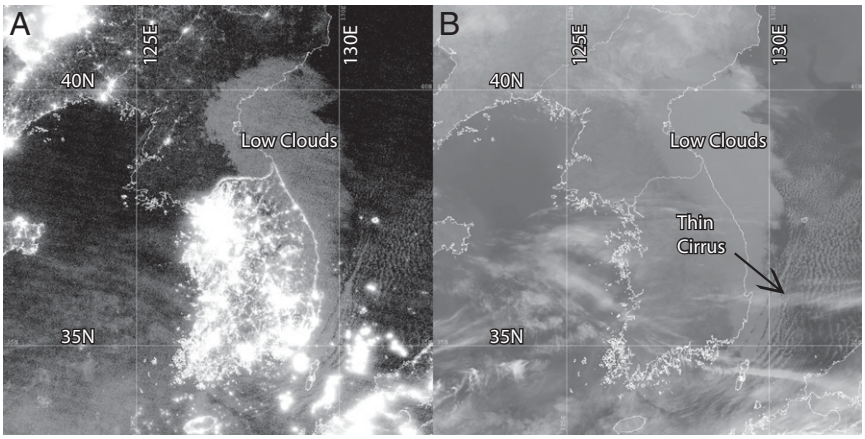

Fig. 4. VIIRS/DNB low-light imagery (*A*) of the Korean Peninsula on the night of February 23, 2012, at 1730 UTC during new moon, showing low clouds on the eastern coast and superior edge contrast over land compared with VIIRS/M15 (10.763 μm) thermal infrared imagery (*B*). Note in particular the western and northern edges of the cloud formation.

leak came from the simple observation that clouds in the tropics appear brighter than the surrounding clear-sky ocean background. This behavior is opposite to the emissive signature expected from cool clouds observed against a warmer underlying surface but consistent with visible light reflectance of clouds observed against a low albedo ocean background.

The imagery in Figs. 1, 4 and 5 appear similar to daytime observations, which reveals synoptic-scale patterns of migratory storm clouds, maritime boundary layer clouds, and tropical convection. One notable difference from daytime imagery, however, is the presence of broad (~1,000 km scale) regions of diffuse brightness. These features, as noted in Fig. 1, are thought to be areas where primary airglow emissions are locally strong enough for the DNB to detect directly. Similar structures were observed on all nights but in different locations. Their scale and distribution are consistent with OGO-4 airglow observations (19).

Other characteristics of the DNB imagery speak to the unique nature of the DIM illumination. Note in Fig. 3 the smooth low-end tail structure that is unique to the new moon distribution. The secondary low-radiance modes seen in the daytime and full moon cases come primarily from the solar and lunar glint regions. The lack of such a glint mode in the new moon distribution is consistent with the extended diffuse nature of the DIM emissions. The pan-horizon illumination from airglow represents a fundamental difference from the highly directional solar/lunar sources in the sense that cloud shadows will be minimized—potentially improving cloud masks.

Concerning the airglow waves observed in Fig. 5, the measured horizontal wavelength of ~33 km is consistent with thunderstorm-induced waves observed by the Midcourse Space Experiment (MSX) midwave-infrared (4.3 μm) limb sounder data (33, 34). Sensitivity to both primary and reflected DIM light sources provides a unique perspective on coupling between the troposphere and mesosphere. Additional examples of these waves compared against thermal infrared imagery are published (Figs. S5–S7). In all cases, the waves were not present in corresponding VIIRS thermal infrared imagery.

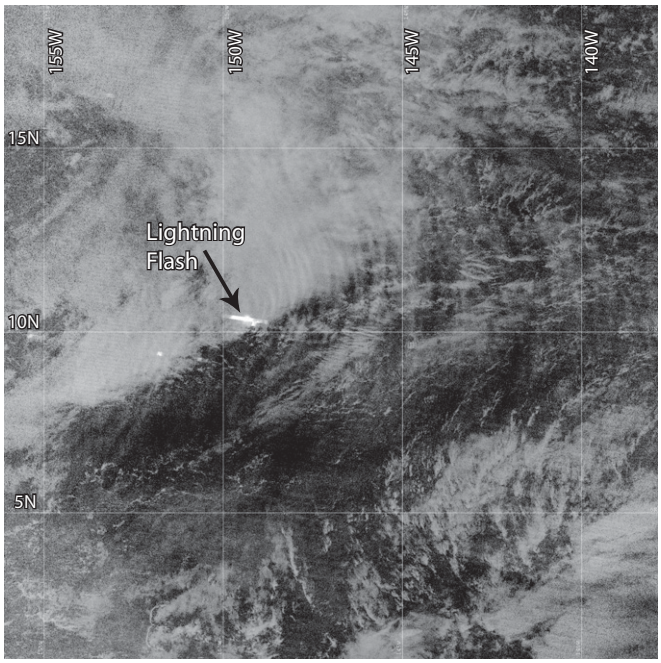

Fig. 5. DNB imagery of thunderstorms (lightning flash indicated) in the tropical central Pacific Ocean on February 22, 2012, at 1107 UTC (a zoomed-in subset of Fig. 2). Airglow waves are evident in the vicinity of the storms. The waves, which have wavelength $\lambda \sim 33$ km, appear to propagate radially outward from the area of convection and extend far beyond the anvil cirrus.

Research and Operational Implications

The information content of most measurements from meteorological satellites falls off markedly at night, particularly with regard to lower tropospheric clouds (owing to poor thermal contrast), which play a key role in defining Earth's energy budget (35). Sensing based on DIM light sources could improve the nocturnal low cloud climatology. In turn, it could improve the fidelity of the sea surface temperature (SST) climate data record that is fundamental to our assessments of climate change, because SSTs are derived from nighttime observations and require a cloud screening that is inherently problematic for low clouds (36). As shown in Fig. 4, the DIM light measurements hold potential to improve nocturnal low cloud masks and, thereby, improve the uncertainty statistics associated with this key climate parameter.

Low clouds and fog also pose significant hazards to transportation by air, land, and sea. At high latitudes, detecting clouds over cold land surfaces and identifying snow and sea ice boundaries are particularly challenging tasks, especially during the winter months when sunlight is unavailable for extended periods. Although multispectral techniques (37–39) in many cases overcome thermal contrast issues in nocturnal low cloud detection, these algorithms face insurmountable difficulties in

the presence of overriding cirrus. DIM light imagery, with its ability to peer through optically thin cirrus layers, holds unique value for overcoming this problem.

Although the VIIRS/DNB has demonstrated the potential of DIM light, future sensors could be optimized to better exploit these signals. For example, geostationary-based sensors could provide the first continuous (24-h) visible light observing capability. Such time-resolved imagery would allow for monitoring primary airglow emissions, including mesospheric wave detection (Fig. 5) in support of tsunami warning systems. Low earth-orbiting satellites such as Suomi NPP must conduct short integration times per sample because of their motion relative to the surface, but with geostationary satellites, the observed scene is essentially fixed, allowing for much longer integration times. This staring capability would help to overcome the weaker signal due to significantly higher geostationary orbital altitudes (35,786 km), which enables imagery with spatial resolution comparable to NPP while providing more frequent updates.

Conclusion

The eyes of Suomi NPP have opened our own to visible-light sources that transcend the darkness and understood limitations of nighttime environmental sensing. The capability of the VIIRS/DNB to detect airglow and starlight illumination holds important and immediate practical implications for climate assessment, weather and hazards monitoring, and our ability to observe interactions between the lower and upper atmosphere. The particular value of airglow, traditionally regarded within the astronomy community as a nuisance, seems to reaffirm the old adage that "One man's trash is another man's treasure." These findings stand to influence the scope and design of next-generation environmental satellite missions.

The complex space/time variability of DIM light sources presents unique research challenges for quantitative applications. Whereas contributions from the integrated starlight and zodiacal light will vary with both local observation time and season in predictable ways, contributions from the airglow include the primary emission. A multisensor approach that incorporates simultaneous, independent observations of the primary airglow emission layer may offer a way to quantify this highly dynamic source.

Methods

To calibrate and quality-control the VIIRS/DNB data, departures from laboratory measurements of the background electronic noise and offset pattern must be characterized and removed (40, 41). The offset for the high gain stage of the DNB was determined by observing the Pacific Ocean during the new moon, when the solar zenith angle was at least 105° (15° below the horizon). Only data between 50° south and 50° north latitude were included to exclude illumination from the aurora. A mask was used to exclude areas of known anthropogenic illumination. Outliers were rejected by using a 3-δ filter.

Nighttime imagery examples were produced from Suomi NPP VIIRS/DNB descending nodes by using data obtained from the NPP Integrated Data Processing Segment. Only new moon data under astronomical dark (solar and lunar zenith angles > 108°) illumination conditions were considered. The noise/offset corrected radiance data were remapped to a Mercator projection, cropped to a maximum satellite zenith angle of 60° to avoid residual edge-of-scan noise patterns, scaled logarithmically between [−11.5, −9.0] $\log(W{\cdot}cm^{-2}{\cdot}sr^{-1})$, and plotted by using a linear grayscale color palette.

Normalized distributions of DNB radiance for new moon, full moon, and daytime scenes were based on data collections over the north/central Pacific Ocean (no land surface reflectance or city light contributions). New moon data were from February 23, 2012 [1404–1422 Coordinated Universal Time (UTC)], full moon from December 7, 2011 (1220–1232 UTC), and daytime from March 10, 2012 (2331–2351 UTC). Total samples in each distribution exceeded 17 million. Noise/offset corrections for the new moon and full moon data, and a factor of two bit-stripping correction for the daytime radiances, were applied. The radiance data for all three cases were cropped at a maximum sensor zenith angle of 60° and logarithmically scaled, binned over the range [−13.0, 0.0] $\log(W{\cdot}cm^{-2}{\cdot}sr^{-1})$ at 0.05 increments, and normalized.

ACKNOWLEDGMENTS. We thank Kohji Tsumura (Institute of Space and Astronautical Science, Japan Aerospace Exploration Agency), Christoph Leinert (Max Planck Institute for Astronomy), and Joachim Köppen (University of Strasbourg) for insight on nighttime light sources; Jody Russell [Image Science and Analysis Laboratory, National Aeronautics and Space Administration (NASA)-Johnson Space Center) and Dr. Donald Pettit [NASA, International Space Station (ISS) Astronaut] for assistance with ISS photography; and Jeffrey Cox (Aerospace, Offutt Air Force Base) for assistance with Defense Meteorological Satellite Program datasets. We acknowledge the support of the Naval Research Laboratory through contract N00173-10-C-2003, the Oceanographer of the Navy through the Program Executive Office C4I/PMW-120 under program element PE-0603207N, and the National Oceanic and Atmospheric Administration Joint Polar Satellite System Cal/Val and Algorithm Program. The views, opinions, and findings in this report are those of the authors, and should not be construed as an official NOAA and/or US Government position, policy, or decision.

1. Ingham MF (1971) The light of the night sky and the interplanetary medium. *Rep Prog Phys* 34:875–912.
2. Roach FE, Gordon JL (1973) *The Light of the Night Sky* (D. Reidel, Dordrecht, The Netherlands).
3. Leinert Ch, et al. (1997) The 1997 reference of diffuse night sky brightness. *Astron Astrophys Suppl Ser* 127:1–99.
4. Croft TA (1978) Night-time images of the earth from space. *Sci Am* 239:68–79.
5. Croft TA (1973) Burning waste gas in oil fields. *Nature* 245:375–376.
6. Welch R (1980) Monitoring urban population and energy utilization patterns from satellite data. *Remote Sens Environ* 9:1–9.
7. Elvidge CD, Baugh KE, Kihn EA, Kroehl HW, Davis ER (1997) Mapping of city lights using DMSP Operational Linescan System data. *Photogramm Eng Remote Sensing* 63: 727–734.
8. Miller SD, Haddock SHD, Elvidge CD, Lee TF (2005) Detection of a bioluminescent milky sea from space. *Proc Natl Acad Sci USA* 102:14181–14184.
9. Salomonson VV, Barnes WL, Maymon PW, Montgomery HE, Ostrow H (1989) MODIS: Advanced facility instrument for studies of the Earth as a system. *IEEE Trans Geosci Rem Sens* 27:145–153.
10. Lee TF, et al. (2006) The NPOESS/VIIRS day/night visible sensor. *Bull Am Meteorol Soc* 87:191–199.
11. Tsumura K, et al. (2010) Observations of the near-infrared spectrum of the zodiacal light with CIBER. *Astrophys J* 719:394–402.
12. Toller GN (1990) Galactic and extragalactic background radiation, optical observations of galactic and extragalactic light: Implications for galactic structure. *Proceedings IAU Symposium 139*, eds Bowyer S, Leinert Ch (Kluwer, Dordrecht, The Netherlands), pp. 21–34.
13. Hoffman W, Lemke D, Thum C (1997) Balloon-borne infrared telescope for absolute surface photometry of the night sky. *Appl Opt* 16:3125–3130.
14. Kwon SM, Hong SS, Weinberg JL (1991) Origin and Evolution of Interplanetary Dust, *Proceedings IAU Symposium 126*, eds Levasseur-Regourd AC, Hasegawa H (Kluwer, Dordrecht, The Netherlands), pp. 179–182.
15. Mende SB, Banks PM, Nobles R, Garriott OK, Hoffman J (1983) Photographic observations of Earth's airglow from space. *Geophys Res Lett* 10:1108–1111.
16. Broadfoot AL, Kendall KR (1968) The Airglow Spectrum, 3100-10,000Å. *J Geophys Res Space Physics* 73:426–428.
17. Meinel AB (1950) OH emission bands in the spectrum of the night sky. *Astrophys J* 111:555.
18. Donahue TM, Guenther B, Thomas R (1973) Distribution of atomic oxygen in the upper atmosphere deduced from Ogo 6 airglow observations. *J Geophys Res* 78: 6662–6689.
19. Reed EI, Fowler WB, Blamont JE (1973) An atlas of low-latitude 6300-Å [O I] night airglow from Ogo 4 Observations. *J Geophys Res* 78:5658–5675.
20. Xu J, et al. (2010) Strong longitudinal variations in the OH nightglow. *Geophys Res Lett* 37:L21801.
21. Cogger LL, Elphistone RD, Murphree JS (1981) Temporal and latitudinal 5577 Å airglow variations. *Can J Phys* 59:1296–1307.
22. Takahashi H, Onohara A, Shiokawa K, Vargas F, Gobbi D (2011) Atmospheric wave induced O_2 and OH airglow intensity variations: effect of vertical wavelength and damping. *Ann Geophys* 29:631–637.
23. Adachi T, et al. (2010) Midnight latitude-altitude distribution of 630 nm airglow in the Asian sector measured with FORMOSAT-2/ISUAL. *J Geophys Res* 115:A09315.
24. Shepherd GG, McLandress C, Solheim BH (1995) Tidal influence on $O(^1S)$ airglow emission rate distributions at the geographic equator as observed by WINDII. *Geophys Res Lett* 22:94GL03052.
25. Marsh DR, Smith AK, Mlynczak MG, Russell JM, III (2006) SABER observations of the OH Meinel airglow variability near the mesopause. *J Geophys Res* 111:A10S05.
26. Hersé M (1984) Waves in the OH emissive layer. *Science. New Series* 225:172–174.
27. Mende SB, Swenson GR, Geller SP, Spear KA (1994) Topside observation of gravity waves. *Geophys Res Lett* 21:2283–2286.
28. Makela JJ, et al. (2011) Imaging and modelling the ionospheric airglow response over Hawaii to the tsunami generated by the Tohoku earthquake of 11 March 2011. *Geophys Res Lett* 38:L00G02.
29. Paxton LJ, et al. (1992) SSUSI: An horizon-to-horizon and limb viewing spectrographic imager – UV remote sensing, *SPIE International Symposium on Optical Applied Science and Engineering, Ultraviolet Technology IV*, SPIE Paper 1764-15.

30. Degenstein DA, Llewellyn EJ, Lloyd ND (2003) Volume emission rate tomography from a satellite platform. *Appl Opt* 42:1441–1450.
31. Warnecke G, et al. (1969) Meteorological results from multi-spectral photometry in airglow bands by the OGO-4 satellite. *J Atmos Sci* 26:1329–1339.
32. Walker DE, Schwarz HE, Bustos E (2006) Monitoring the night sky with the Cerro Tololo all-sky camera for the TMT and LSST projects. *Proc SPIE* 6267:62672O.
33. Taylor MJ, Hapgood MA (1988) Identification of a thunderstorm as a source of short period gravity waves in the upper atmospheric nightglow emissions. *Planet Space Sci* 36:975–985.
34. Dewan EM, et al. (1998) MSX satellite observations of thunderstorm-generated gravity waves in mid-wave infrared images of the upper stratosphere. *Geophys Res Lett* 25:939–942.
35. Stephens GL (2005) Cloud feedbacks in the climate system: A critical review. *J Clim* 18: 237–273.
36. Patrenko B, Ignatov A, Kihai Y, Heidinger A (2010) Clear-sky mask for the advanced clear-sky processor for oceans. *J Atmos Ocean Technol* 27:1609–1623.
37. Lee TF (2000) Nighttime observation of sheared tropical cyclones using GOES 3.9-μm data. *Weather Forecast* 15:759–766.
38. Ellrod GP (1995) Advances in the detection and analysis of fog at night using GOES multispectral infrared imagery. *Weather Forecast* 10:606–619.
39. Pavolonis MJ (2010) Advances in extracting cloud composition information from spaceborne infrared radiances—a robust alternative to brightness temperatures. Part I: Theory. *J Appl Meteorol Climatol* 49:1992–2012.
40. Mills S, et al. (2010) *Calibration of the VIIRS Day/Night Band (DNB). American Meteorological Society 6th Annual Symposium on Future National Operational Environmental Satellite Systems-NPOESS and GOES-R, 9.4* (American Meteorological Society, Boston). CD-ROM..
41. Jacobson E, et al. (2010) Operation and characterization of the Day/Night Band (DNB) for the NPP Visible/Infrared Imager Radiometer Suite (VIIRS). *American Meteorological Society 6th Annual Symposium on Future National Operational Environmental Satellite Systems-NPOESS and GOES-R* (American Meteorological Society, Boston), P349.